Cryogenic probe technology enables multidimensional solid-state NMR of the stratum corneum without isotope labeling

Downloaded from: https://research.chalmers.se, 2024-11-05 08:31 UTC

Citation for the original published paper (version of record):
Perrone, B., Gunnarsson, M., Bernin, D. et al (2024). Cryogenic probe technology enables multidimensional solid-state NMR of the stratum corneum without isotope labeling. Solid State Nuclear Magnetic Resonance, 134. http://dx.doi.org/10.1016/j.ssnmr.2024.101972

N.B. When citing this work, cite the original published paper.

research.chalmers.se offers the possibility of retrieving research publications produced at Chalmers University of Technology. It covers all kind of research output: articles, dissertations, conference papers, reports etc. since 2004. research.chalmers.se is administrated and maintained by Chalmers Library

(article starts on next page)

Solid State Nuclear Magnetic Resonance 134 (2024) 101972

Contents lists available at ScienceDirect

Solid State Nuclear Magnetic Resonance

journal homepage: www.elsevier.com/locate/ssnmr

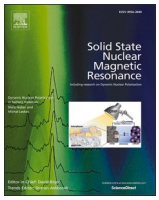

Cryogenic probe technology enables multidimensional solid-state NMR of the *stratum corneum* without isotope labeling

Barbara Perrone [a], Maria Gunnarsson [b], Diana Bernin [c], Emma Sparr [b], Daniel Topgaard [b,*]

[a] *Bruker Biospin, Fällanden, Switzerland*
[b] *Department of Chemistry, Lund University, Lund, Sweden*
[c] *Department of Chemistry and Chemical Engineering, Chalmers University of Technology, Göteborg, Sweden*

ARTICLE INFO

Handling Editor: Prof D Bryce

ABSTRACT

Solid-state NMR has great potential for investigating molecular structure, dynamics, and organization of the *stratum corneum*, the outer 10–20 μm of the skin, but is hampered by the unfeasibility of isotope labelling as generally required to reach sufficient signal-to-noise ratio for the more informative multidimensional NMR techniques. In this preliminary study of pig *stratum corneum* at 35 °C and water-free conditions, we demonstrate that cryogenic probe technology offers sufficient signal boost to observe previously undetectable minor resonances that can be uniquely assigned to fluid cholesterol, ceramides, and triacylglycerols, as well as enables ^{1}H–^{1}H spin diffusion monitored by 2D ^{1}H-^{13}C HETCOR to estimate 1–100 nm distances between specific atomic sites on proteins and lipids. The new capabilities open up for future multidimensional solid-state NMR studies to answer long-standing questions about partitioning of additives, such as pharmaceutically active substances, between solid and liquid domains within the protein and lipid phases in the *stratum corneum* and the lipids of the sebum.

1. Introduction

The excellent mechanical and barrier properties of the human skin originate from its outermost 10-20 μm—the *stratum corneum*—comprising stacks of keratin-filled dead cells, known as corneocytes, embedded in a matrix of lipids in a structure resembling brickwork as illustrated in Fig. 1 [1,2]. Within the corneocytes, the keratin filaments form a dense network with sufficient mechanical strength to keep the hydrophobic barrier of the extracellular lipid matrix intact under compression, bending, and tension [3]. The *stratum corneum* lipids consist of an approximately equimolar mixture of cholesterol, free fatty acids, and ceramides organized into an intricate multilayer structure with aligned and mostly crystalline hydrocarbon chains [4,5].

Building on pioneering works by Jokura et al. [6], we have through a series of ^{13}C MAS NMR studies relying on spectral editing by CP and INEPT for selective detection of solid and liquid molecular segments [7,8] elucidated the molecular-scale underpinnings of the macroscopic barrier and mechanical properties, revealing co-existence of solid and fluid lipid phases as well as solid and dissolved protein filaments with proportions determined by hydration [9,10], temperature [11], and the presence of additives acting as moisturizers in cosmetics applications [12–15], penetration enhancers in drug delivery [16–18], or solvents in cleaning products [19]. Since the raw material for these studies is *stratum corneum* from pig or human skin, ^{13}C isotope labelling of the protein or lipid components is not an option, and even basic 1D ^{13}C spectroscopy may require 12 h of measurement time to reach sufficient signal-to-noise to determine the dynamic state of the major protein and lipid components.

To get more detailed information about molecular dynamics and organization of the *stratum corneum* lipids, numerous studies have employed model systems comprising various well-defined mixtures of free fatty acids, cholesterol, and ceramides. Early X-ray studies led to the proposal of the sandwich model with alternating layers of fluid and crystalline solid lipids [20–22]. The fluid component was later attributed to the unsaturated acyl chain of the ceramide Cer[EOS], see Fig. 1b, using ^{13}C MAS and ^{1}H diffusion NMR targeting the distinct chemical shifts of the double bonds [23], ^{2}H wideline and ^{13}C MAS NMR on a series a mixtures with specifically ^{2}H- or ^{13}C-labeled lipids [24–27], and all-atom molecular dynamics simulations [28]. So far, these detailed results from model systems have not been confirmed for lipids within the *stratum corneum*, chiefly because of the challenges to reach sufficient sensitivity to detect the crucial resonances under the constraint of

* Corresponding author.
E-mail address: daniel.topgaard@fkem1.lu.se (D. Topgaard).

https://doi.org/10.1016/j.ssnmr.2024.101972
Received 15 May 2024; Received in revised form 19 August 2024; Accepted 20 September 2024
Available online 21 September 2024
0926-2040/© 2024 The Authors. Published by Elsevier Inc. This is an open access article under the CC BY license (http://creativecommons.org/licenses/by/4.0/).

natural isotopic abundance and dilution by the protein components forming the major part of the intact biological material.

While cryogenic probe technology has become standard for biomolecular applications of high-resolution solution NMR [29], it has only recently been implemented in the context of solid-state NMR, offering sensitivity enhancement of a factor 3–4 compared to conventional room-temperature probes under otherwise identical conditions [30–32]. Here we investigate the potential benefits of cryogenic probe technology for *stratum corneum* studies, demonstrating detection of lipid type-specific minor resonances that have previously only been accessible in concentrated model lipid systems, as well as application of ^{1}H–^{1}H spin diffusion with 2D ^{1}H-^{13}C HETCOR detection to estimate 1–100 nm distances between specific atomic sites in the proteins and lipids, thereby paving the way for future studies to pinpoint the locations and dynamics of moisturizers, penetration enhancers, and solvents in the intricate composite structure with solid and fluid lipid domains and solid and dissolved protein filaments.

2. Materials and methods

A batch of *stratum corneum* powder slightly contaminated with sebum lipids was prepared using >20 pairs of pig ears from a south Swedish (Scania province) abattoir. The ears were washed from excess contaminants using cold water, dried, and shaved. Slices from the insides of the ears were cut to 0.5 mm thickness with a dermatome. To detach the *stratum corneum* from the underlying tissue, the slices were placed on filter paper saturated with 0.2 % (w/v) bovine pancreas trypsin type III (Sigma-Aldrich Chemie GmbH, Schnelldorf, Germany) in phosphate buffered saline (NaCl, $Na_2HPO_4{\cdot}2H_2O$, KH_2PO_4 used as purchased from Merck), wrapped in aluminum foil, and stored at 4 °C. After 24 h, the *stratum corneum* was removed with forceps, washed thoroughly in Milli-Q water, vacuum dried to allow later control of hydration level by addition of known amounts of water, and placed in −20 °C to prevent biological and chemical degradation during months of storage. Effects of biological variations between individual animals were reduced by grinding the dry *stratum corneum* sheets from all >20 pairs of ears to a single batch of powder. Samples from this batch were tightly packed into 3.2 mm cryoprobe and 4 mm HR-MAS rotors (both from Bruker) with, respectively, 90 and 50 μL volumes sealed with Kel-F plugs to prevent leakage of fluid lipids during MAS. The larger sample volume for the cryoprobe rotor results from its unusual length. As a reference for triacylglycerols in the sebum lipids, *Griebenschmalz* from a southwest German (Swabia province) butcher shop was put into a disposable HR-MAS rotor insert with 40 μL sealed sample volume and transferred to a 4 mm rotor.

NMR measurements were performed on Bruker Avance-Neo spectrometers equipped with a 14.1 T magnet and a 3.2 mm HCN MAS CryoProbe or a 11.7 T magnet and 4 mm Efree HCP MAS or 4 mm HX CP MAS probe. 1D^{13}C spectra were recorded at 12 kHz MAS with the DP, ramped CP [36,37], and refocused INEPT [38,39] pulse sequences for dynamics-based spectral editing [7,8]. CP was carried out with 60 kHz ^{13}C and from 80 to 40 kHz ramped ^{1}H nutation frequencies during 1 ms contact time τ_{CP}, while INEPT employed delays of 1.8 and 1.2 ms duration. For the cryoprobe, the DP sequence was augmented with a 166 μs spin echo to minimize baseline distortions from probe ringings. With these acquisition parameters, INEPT yields signal for C-H bonds with reorientational correlation time τ_c lower than ~10 ns and orientational order parameter $|S_{CH}|$ smaller than ~0.2 [8,40]. CP is roughly complementary to INEPT, with the exception of the anisotropic liquid regime, $\tau_c < 10$ ns and $|S_{CH}| \approx 0.1$, where both CP and INEPT are efficient, and the intermediate regime, $\tau_c \approx 1$ μs, where signal is only observed with DP. In the context of this paper, the presence of CP or INEPT signals constitutes an operational definition of "solid" and "liquid" molecules or molecular segments, which should be understood in terms of C-H bond reorientation and the quantitative conditions on τ_c and $|S_{CH}|$ given above. Correspondingly, 2D ^{1}H-^{13}C HETCOR data was acquired with either CP or INEPT, the former additionally also as a function of τ_{CP} (eight values from 62.5 μs to 8 ms in a geometric sequence) and ^{1}H–^{1}H spin diffusion time τ_{SD} (six values from 12.5 ms to 0.8 s in a geometric sequence) inserted as a time of longitudinal storage between ^{1}H chemical shift evolution and ^{1}H-^{13}C CP [41]. Additional acquisition parameters are reported in the figure captions.

Analysis of spin diffusion data was performed with a two-phase (source A and sink B) lamellar model with domain widths d_A and d_B, spin densities ρ_A and ρ_B, and spin diffusion coefficients D_A and D_B, where the approach of the normalized signal intensity I_B towards unity as a function of effective mixing time $\tau_m = (0.5\tau_{CP} + \tau_{SD})$ [42] can be written as [43].

$$I_B(\tau_m) = 1 - \sum_{n=1}^{\infty} w_n \exp(-\Gamma_n \tau_m), \quad (1)$$

where

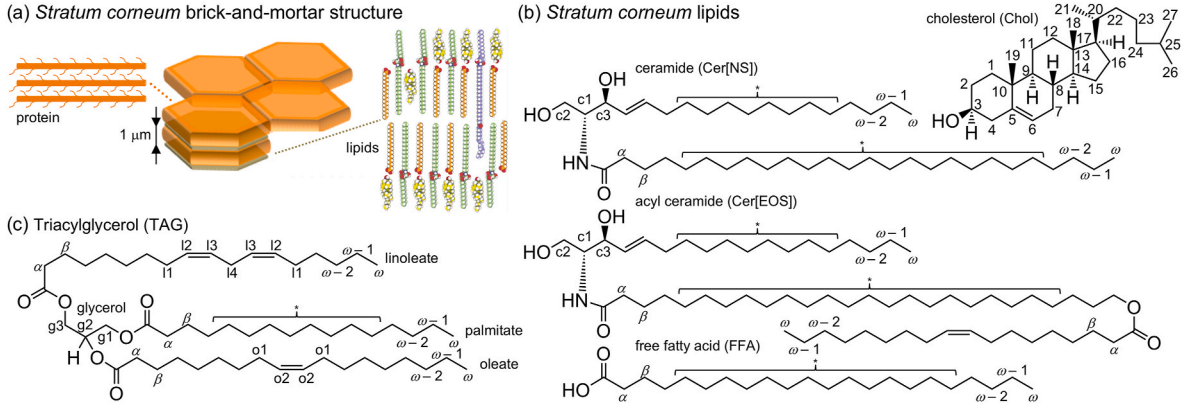

Fig. 1. Schematic structure of *stratum corneum* and representative molecules. (a) "Brick-and-mortar" structure of protein-filled corneocytes embedded in a multilayer lipid matrix. The corneocytes have 25–45 μm diameters [33], 0.8–1 μm thickness [34], and are separated by a lipid matrix of 80–100 nm thickness [35]. (b) Typical *stratum corneum* lipids with labeling of carbon atoms that give distinct ^{13}C NMR signals. (c) Example of triacylglycerol (TAG) that constitutes the largest fraction of sebum and subcutaneous fat lipids and may occur as a contaminant in *stratum corneum* preparations. The overbraces point out interior CH_2 groups that are often unresolved in the NMR spectra. NMR signals from acyl chain carbons α, β, (ω–2), (ω-1), ω, o1, o2, l1, l2, l3, and l4 may originate from many lipid types. Each of TAG, Cer, and Chol give unique signals (TAG: g1-g3; Cer: c1-c3, C=C; Chol: most of the 27 carbons). Natural *stratum corneum* and sebum lipids comprise broad distributions of chain lengths and degrees of unsaturation. Panel a adapted from Refs. [5,11] with permission.

$$w_n = 8\frac{\Gamma_A\Gamma_B}{\Gamma_n}\bullet\frac{\cos\left(\sqrt{\Gamma_n}\sqrt{\tau_+}\right)-\cos\left(\sqrt{\Gamma_n}\sqrt{\tau_-}\right)}{C_+\cos\left(\sqrt{\Gamma_n}\sqrt{\tau_+}\right)-C_-\cos\left(\sqrt{\Gamma_n}\sqrt{\tau_-}\right)}, \quad (2)$$

$$\sqrt{\tau_\pm}=\frac{\sqrt{\Gamma_B}\pm\sqrt{\Gamma_A}}{2\sqrt{\Gamma_A\Gamma_B}}, \quad (3)$$

$$C_\pm = X_A\Gamma_A + X_B\Gamma_B \pm \sqrt{\Gamma_A\Gamma_B}, \quad (4)$$

$$X_A=\frac{\rho_A d_A}{\rho_A d_A+\rho_B d_B}, \quad X_B = 1 - X_A, \quad (5)$$

$$\sqrt{\Gamma_A}=\frac{\sqrt{D_A}}{d_A}, \quad \sqrt{\Gamma_B}=\frac{\sqrt{D_B}}{d_B}, \quad (6)$$

and $\sqrt{\Gamma_n}$ are the roots of

$$\sqrt{\tau_+^*}\sin\left(\sqrt{\Gamma_n}\sqrt{\tau_+}\right)+\sqrt{\tau_-^*}\sin\left(\sqrt{\Gamma_n}\sqrt{\tau_-}\right)=0 \quad (7)$$

where

$$\sqrt{\tau_\pm^*}=\frac{\sqrt{\pi}}{4}\bullet\frac{X_A\sqrt{\Gamma_A}\pm X_B\sqrt{\Gamma_B}}{\sqrt{\Gamma_A\Gamma_B}}. \quad (8)$$

The equations above are here written in a somewhat unconventional way to highlight that the six parameters $[d_A,d_B,\rho_A,\rho_B,D_A,D_B]$ can for data fitting purposes be condensed into no more than three independent ones: the molar fraction X_A and the intra-phase equilibration rates Γ_A and Γ_B, which also via Eq. (8) define the characteristic equilibration time τ_+^* in the initial-rate approximation [44]:

$$\lim_{\tau_m\to 0} I_B(\tau_m)=\frac{\sqrt{\tau_m}}{\sqrt{\tau_+^*}}. \quad (9)$$

To minimize the influence of T_1 relaxation on the fit results, the normalized peak intensity I_B in Eq. (1) is calculated from the 2D ^{1}H-^{13}C HETCOR spectra as the equilibration percentage obtained from the exchange and source peaks at a single selective ^{1}H shift and across the full unselective ^{1}H projection as proposed and described in detail in Ref. [45].

3. Results and discussion

Fig. 2 illustrates the signal boost offered by the 3.2 mm cryoprobe at 14.1 T relative to the 4 mm Efree probe at 11.7 T by comparing 1D ^{13}C spectra of the dry sebum-containing *stratum corneum*. While the spectra normalized to the same maximum signal amplitude superficially seem similar, the magnifications to roughly the same baseline noise levels reveal dramatic differences, where the cryogenic probe enables detection of INEPT resonances that are unique for fluid cholesterol, ceramides, and triacylglycerols. The sensitivity enhancement observed in Fig. 2 may be attributed to differences in probe technology (cryo vs.

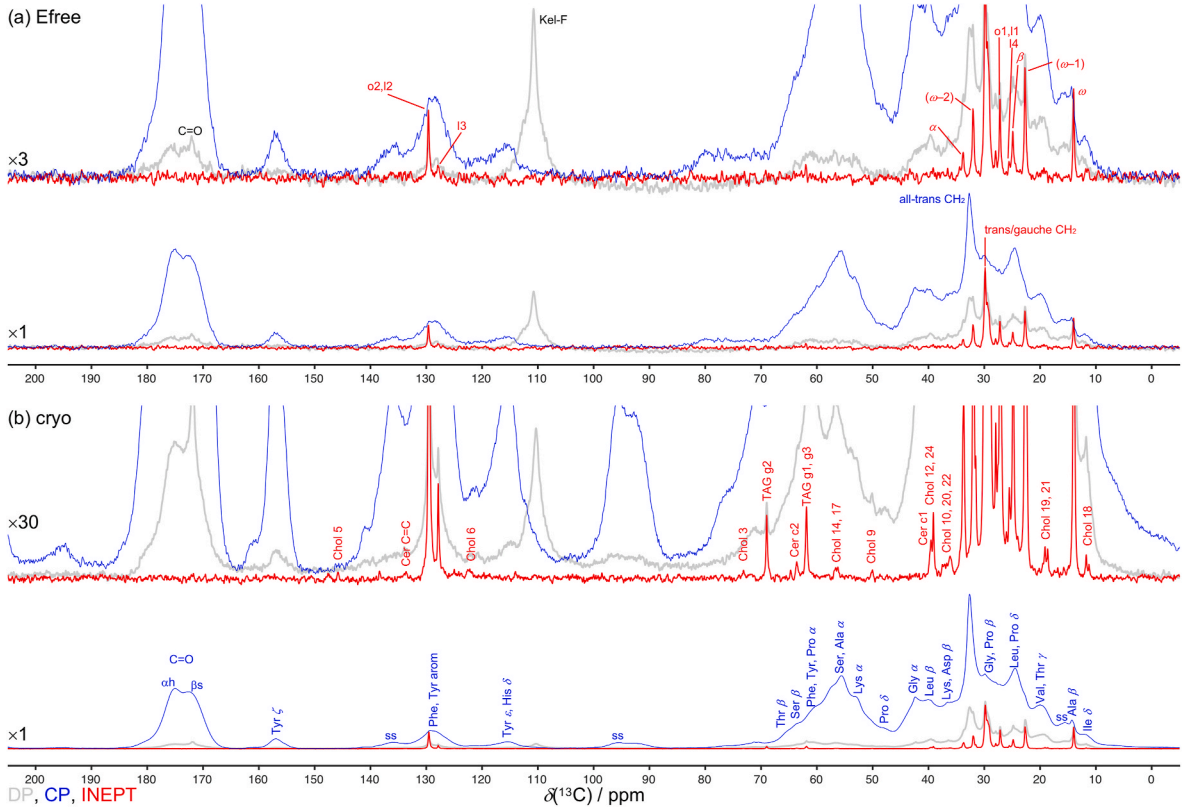

Fig. 2. Cryogenic probe technology enables detection of minor peaks that can be uniquely assigned to specific *stratum corneum* and sebum lipid classes. 1D ^{13}C spectra of dry sebum-containing *stratum corneum* at 35 °C acquired with DP (gray), CP (blue), and INEPT (red) pulse sequences at 12 kHz MAS, 62 kHz SPINAL64 [46] ^{1}H decoupling, 2048 scans, 5 s recycle delay, and 3 h measurement time per spectrum using (a) Efree probe, 125 MHz ^{13}C Larmor frequency, and 4 mm 50 μL HR-MAS rotor and (b) cryoprobe, 150 MHz ^{13}C Larmor frequency, and 3.2 mm 90 μL rotor. For each probe type, the lower panels show DP, CP, and INEPT spectra jointly scaled to the same overall maximum intensity, while the upper panels are vertically scaled with factors of × 3 and × 30, respectively, to approximately the same noise levels of the baselines. The Efree probe yields INEPT signals for acyl chains that may reside on many lipid types, while the cryoprobe enables detection of numerous peaks that can be uniquely assigned to cholesterol (Chol) [47,48], ceramides (Cer) [49], and triacylglycerols (TAG) [50]. Lipid peak assignments refer to the chemical structures in Fig. 1. The labels "all-trans CH_2" and "trans/gauche CH_2" indicate the characteristic signals from interior CH_2 groups in, respectively, solid and molten hydrocarbon chains [51]. Kel-F in the rotor sealing plugs give rise to the DP peaks at 110 ppm. The bottom panel shows CP peak assignments to amino acid carbons including C=O groups in α-helix (αh) and β-sheet (βs) secondary structure [52,53]. Spinning sidebands are indicated with "ss".

Efree) as well as magnetic field (14.1 vs. 11.7 T) and sample volume (90 vs. 50 μL). Consistent with previous studies [30–32], signal-to-noise analysis of the major peaks detectable on both probes yields improvement factors in the range (average) 3.4–5.8 (4.7) for DP, 4.0–8.3 (5.2) for CP, and 4.5–7.8 (5.5) for INEPT after correction for the magnetic field and sample volume. We note that far greater increases in signal-to-noise ratios could be achieved with dynamic nuclear polarization technology [54], however at the expense of having to perform the measurements with the sample at biologically less relevant temperatures, where all lipids are frozen solid, and in the presence of radicals and solvents such as glycerol known to induce phase transitions in the protein and lipid components [12].

The triacylglycerol lipid class is normally not found within the *stratum corneum* structure, but may occur as an impurity from insufficient removal of sebum lipids during sample preparation. The peak assignment to fluid triacylglycerols is verified in Fig. 3, showing 2D ^{1}H-^{13}C INEPT HETCOR of *stratum corneum* and a reference sample of the Swabian food product *Griebenschmalz* containing highly concentrated triacylglycerols rendered from pig fat by dry heating [50]. Although all the peaks of the reference are present also for the *stratum corneum*, only the g1, g2, and g3 signals uniquely distinguish triacylglycerols from ceramides and free fatty acids.

The segregation of proteins and lipids into domains is investigated by ^{1}H–^{1}H spin diffusion detected by 2D ^{1}H-^{13}C CP HETCOR as shown in Fig. 4. The data in panel a was obtained with short cross polarization contact time τ_{CP} (0.25 ms) and vanishing spin diffusion time τ_{SD} and thus features correlation peaks mainly for covalently bonded ^{1}H-^{13}C pairs as well as from protein N**H** and C$_\alpha$**H** to neighboring **C**=O. Increasing τ_{CP} to 2 ms yields a prominent N**H**→**C**$_\alpha$H peak (panel b) and may include ^{1}H–^{1}H relayed correlation peaks for ^{1}H-^{13}C pairs separated by distances approaching a few nanometers. Internal equilibration of the ^{1}H magnetization within the protein phase is evidenced by nearly identical ^{13}C slices at the C$_\alpha$**H** and N**H** ^{1}H shifts as well as ^{1}H slices at the **C**=O (α-helix) and **C**$_\alpha$H ^{13}C shifts (green and blue in panel b). Conversely, the ^{13}C slice at the C**H**$_2$ ^{1}H shift and ^{1}H slice at the **C**H$_2$ ^{13}C shift (red) remain distinctly different from the other slices, proving that the lipids are physically separated from the proteins over distances of at least several nanometers. At τ_{SD} = 0.8 s (panel c), the spectrum includes a distinct N**H**→**C**H$_2$ correlation peak representing long-range intermolecular protein-lipid contacts over distances up to a few hundred nanometers [45]. The similarity of all slices (red, green, and blue) and projections (gray) in the ^{13}C and ^{1}H dimensions indicate nearly complete equilibration of the ^{1}H magnetization between the protein and lipid phases and that at least one of them have minimum dimensions of less than a few hundred nanometers.

The qualitative information about domain sizes from visual inspection of the 2D spectra and 1D slices can be made more quantitative by analysis of the evolution of correlation peak intensities with the effective mixing time $\tau_m = (0.5\tau_{CP} + \tau_{SD})$ [42] using the two-phase lamellar model in panel d and the corresponding Eq. (1) [43] in the methods section. For the quantitative analysis we focus on the distinct and reasonably well-resolved N**H**→**C**$_\alpha$H and N**H**→**C**H$_2$ correlation peaks representing intramolecular protein→protein and intermolecular protein→lipid contacts, respectively. Whereas N**H**→**C**$_\alpha$H is fully

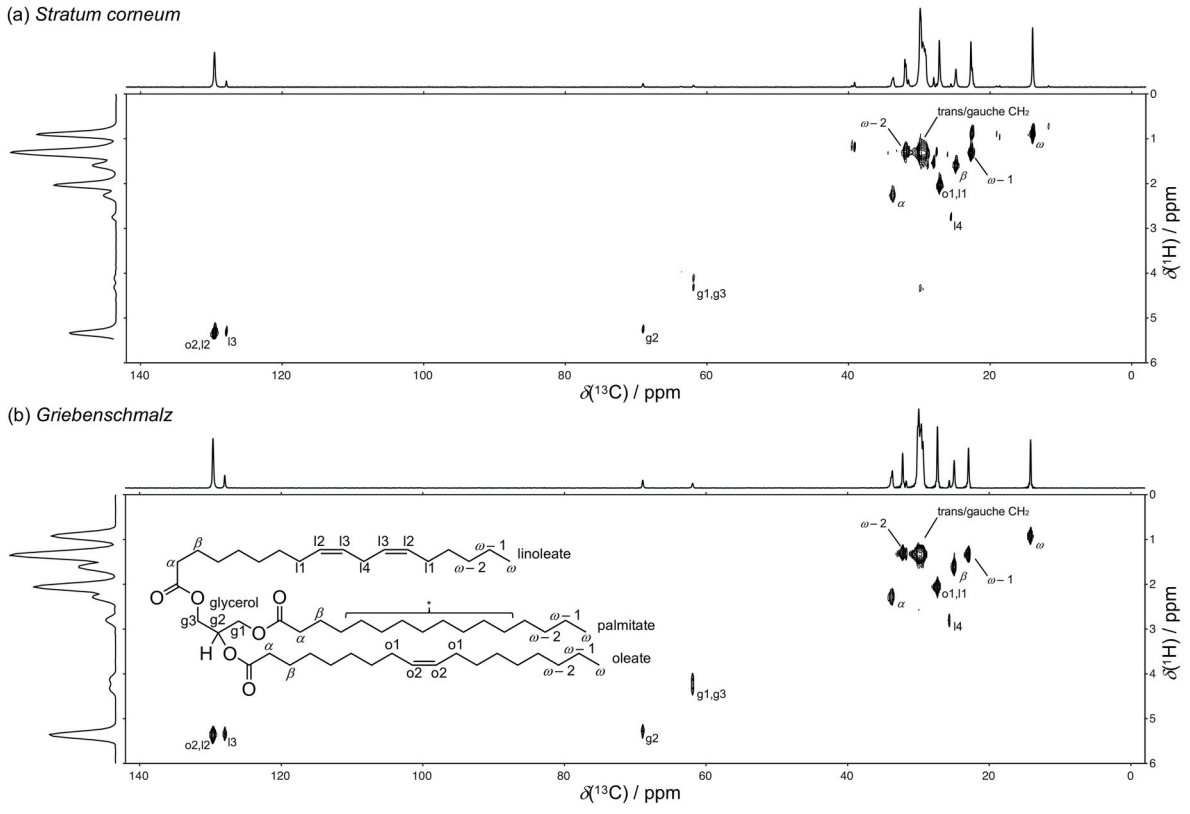

Fig. 3. Validation of *stratum corneum* peak assignment to g1, g2, and g3 carbons unique for triacylglycerols. 2D ^{1}H-^{13}C INEPT HETCOR of fluid components in (a) dry *stratum corneum* at 35 °C and (b) pork crackling embedded in lard at 2 °C (Swabian food product *Griebenschmalz*). Data in panel a was acquired with a 3.2 mm cryoprobe at 150 MHz ^{13}C Larmor frequency, 12 kHz MAS, 6 ppm ^{1}H spectral width, 128 t_1 increments, 150 ppm ^{13}C spectral width, 200 ms acquisition time, 62 kHz SPINAL64 ^{1}H decoupling, 64 scans, 2 s recycle delay, and 5.0 h total measurement time, while the data in panel b was obtained with a 4 mm CP MAS probe at 125 MHz ^{13}C Larmor frequency, 5 kHz MAS, 10 ppm ^{1}H spectral width, 128 t_1 increments, 400 ppm ^{13}C spectral width, 50 ms acquisition time, 62 kHz SPINAL64 ^{1}H decoupling, 32 scans, 2 s recycle delay, and 2.3 h total measurement time. Identical assignments in panels a and b highlight peaks characteristic of triacylglycerols, with all carbons except g1, g2, and g3 being present also in ceramides and free fatty acids, see Fig. 1. Unlabeled peaks in panel a originate from cholesterol and ceramides. The *stratum corneum* sample has at least an order of magnitude lower triacylglycerol concentration than the *Griebenschmalz*.

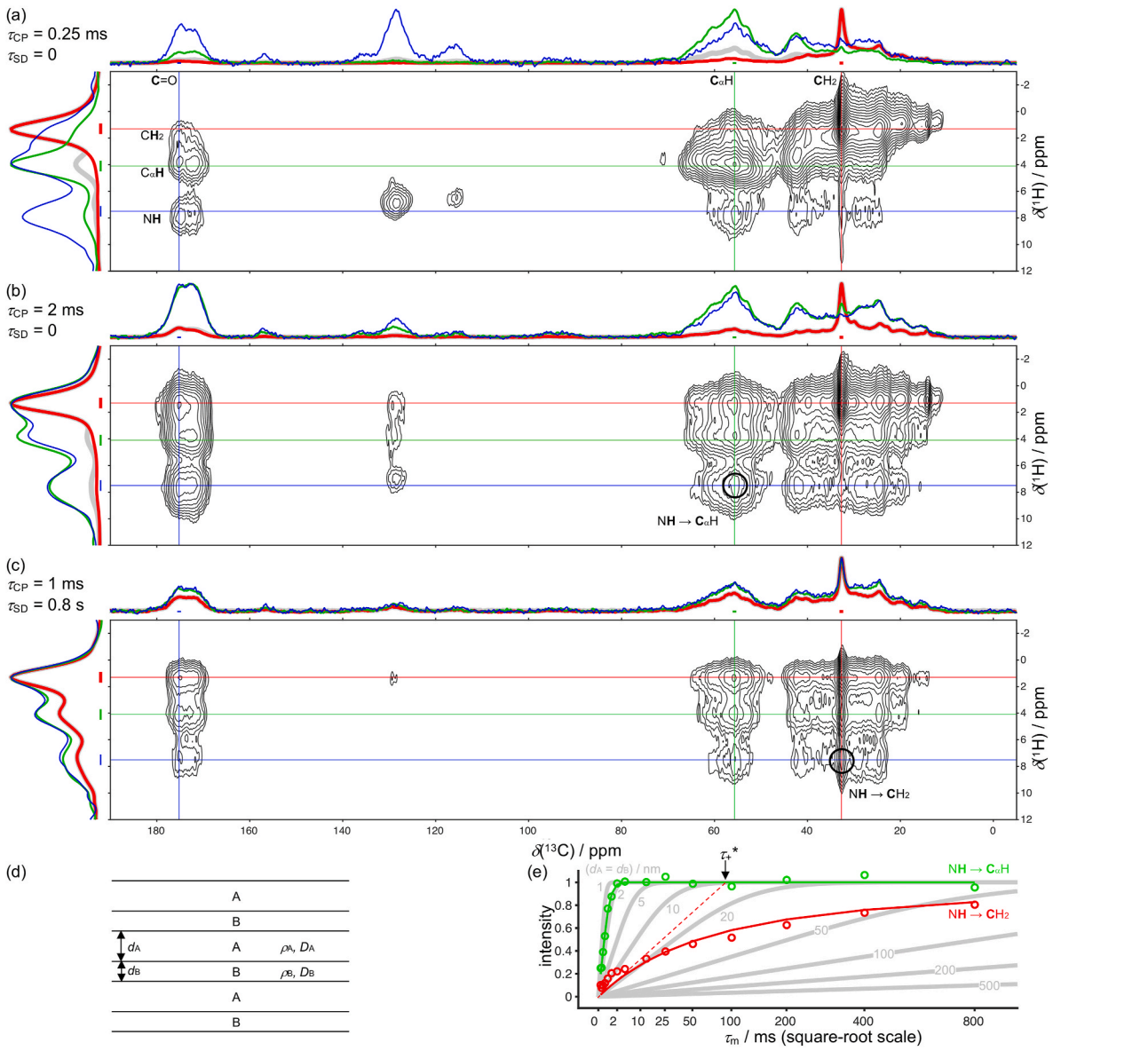

Fig. 4. Cryogenic probe technology enables estimation of 1–100 nm scale interatomic distances within and between molecules in *stratum corneum*. ^{1}H–^{1}H spin diffusion detected via 2D ^{1}H-^{13}C CP HETCOR using a 3.2 mm cryoprobe at 150 MHz ^{13}C Larmor frequency, 12 kHz MAS, 100 kHz FSLG [55] ^{1}H–^{1}H homonuclear decoupling, 40 ppm ^{1}H spectral width, 96 t_1 increments, 390 ppm ^{13}C spectral width, 20 ms acquisition time, 100 kHz SPINAL64 [46] ^{1}H decoupling, 16 scans, 2 s recycle delay, and 52 min measurement time per combination of cross-polarization contact time τ_{CP} and spin diffusion time τ_{SD}. (a) Short τ_{CP} (0.25 ms) and vanishing τ_{SD}. Slices (red, green, and blue) along the ^{1}H and ^{13}C dimensions are obtained at ^{1}H shifts corresponding to lipid C**H**$_2$, protein C$_\alpha$**H**, and protein N**H**, as well as ^{13}C shifts representative of protein **C**=O (α-helix), protein **C**$_\alpha$H, and lipid **C**H$_2$, with integration over narrow frequency intervals as indicated with line segments along the ^{1}H and ^{13}C axes. The slices and projections (gray) are individually scaled to the same maximum intensity. (b) Long τ_{CP} (2 ms) and vanishing τ_{SD} with N**H**→**C**$_\alpha$H correlation peak (circled). (c) Intermediate τ_{CP} (1 ms) and long τ_{SD} (0.8 s) with N**H**→**C**H$_2$ correlation peak (circled). (d) Two-phase lamellar spin diffusion model comprising an infinite stack of alternating layers of A and B domains with widths d_A and d_B, spin densities ρ_A and ρ_B, and spin diffusion coefficients D_A and D_B. (e) Normalized correlation peak intensity [45] vs. effective mixing time $\tau_m = (0.5\tau_{CP} + \tau_{SD})$ [42] for N**H**→**C**$_\alpha$H (green) and N**H**→**C**H$_2$ (red) representative of, respectively, intramolecular protein-protein and intermolecular protein-lipid contacts. The data points are extracted from fourteen 2D ^{1}H-^{13}C CP HETCOR spectra recorded during 12.1 h measurement time. Gray lines are calculated with Eq. (1) for the two-phase lamellar spin diffusion model with $\rho_A = \rho_B$, $D_A = D_B = 0.6$ nm^2/ms, and a series of values of $d_A = d_B$ as labeled in the figure. Green and red lines represent three-parameter fits of Eq. (1) to the experimental data using the molar fraction X_A and intra-domain equilibration rates Γ_A and Γ_B, see Eqs. (5) and (6), as adjustable parameters, yielding characteristic equilibration times τ_+*, defined in Eq. (8), of 0.81 ± 0.04 ms and 84 ± 12 ms (median ± interquartile range) for the two cases, the latter indicated with dashed red line according to initial-rate approximation in Eq. (9).

equilibrated to unity in less than 2 ms, the N**H**→**C**H$_2$ peak has only reached the value 0.8 at the maximum investigated time 800 ms. Comparison of the experimental data with equilibration curves calculated for a two-phase (A and B) lamellar model with equal domain widths $d_A = d_B$ and spin densities $\rho_A = \rho_B$, as well as assumed spin diffusion coefficients of $D_A = D_B = 0.6$ nm^2/ms [44], reveals that the N**H**→**C**H$_2$ distance is at least an order of magnitude larger than for N**H**→**C**$_\alpha$H. Furthermore, the shape of the N**H**→**C**H$_2$ equilibration curve is distinctly different from the calculated symmetric cases, suggesting pronounced asymmetry in domain widths consistent with the *stratum corneum* schematic in Fig. 1a.

Fitting Eq. (1) to the data using the molar fraction $X_A = \rho_A d_A/(\rho_A d_A + \rho_B d_B)$ and the intra-domain equilibration rates $\Gamma_A = D_A/d_A^2$ and $\Gamma_B = D_B/d_B^2$ as adjustable parameters yields satisfactory agreement between theory and experiment, but also illustrates the challenges of pinpointing the origin of the asymmetry. Uncertainty estimation using

bootstrap resampling with replacement [56] shows that multiple sets of $[X_A,\Gamma_A,\Gamma_B]$, where the individual values may vary over several orders of magnitude, all provide equally good fits to the data. Combining X_A, Γ_A, and Γ_B into the effective equilibration time τ_+* according Eq. (8) yields a parameter with acceptable precision: τ_+* = 0.81 ± 0.04 ms (median ± interquartile range) for N**H**→**C**$_\alpha$H and 84 ± 12 ms for N**H**→**C**H$_2$. This parameter could also be estimated with initial-rate approximation [44] and corresponds to the value of τ_m where the initial straight equilibration line reaches an intensity of 1 as shown in panel e. The factor 100 longer value of τ_+* for N**H**→**C**H$_2$ (intermolecular protein→lipid) than N**H**→**C**$_\alpha$H (intramolecular protein→protein) corresponds to roughly a factor $(100)^{1/2} = 10$ longer minimum distance between the involved nuclei consistent with the structure in Fig. 1. Determination of actual distances would require independent information about the values of ρ_A, ρ_B, D_A, and D_B, the latter being accessible for instance by augmenting the 2D ^{1}H-^{13}C CP HETCOR sequence with a ^{1}H CPMG dimension [57], which is beyond the scope of this work but well within the capabilities offered by the cryoprobe.

4. Conclusions and outlook

The cryogenic probe technology offers improvements in signal-to-noise ratio that is clearly demonstrated by allowing detection of resonances that are hidden in the noise for data acquired on a more conventional Efree probe under similar experimental conditions. For *stratum corneum* studies, some of these new peaks are particularly valuable because they can be unambiguously assigned to cholesterol, ceramides, and triacylglycerols, the latter most likely being present as a sebum lipid rather than an integral part of the protein-lipid "brick-and-mortar" structure. With improved sensitivity, previously unfeasible multidimensional techniques may be applied as here demonstrated by some rather basic 2D ^{1}H-^{13}C INEPT HETCOR to validate the fluid lipid peak assignments and ^{1}H–^{1}H spin diffusion detected via 2D ^{1}H-^{13}C CP HETCOR to estimate 1–100 nm scale distances between specific types of solid protein and lipid atoms. Future extensions of this approach could be to implement dynamic filters to follow spin diffusion (or relayed NOEs for liquids) from ^{1}H nuclei in liquid environments to ^{13}C in solids or vice versa to pinpoint the locations of the fluid lipids or pharmaceutically active substances within the otherwise mainly solid protein-lipid composite material. Furthermore, the dynamics of the small fraction of fluid lipids could be investigated more in detail by measurements of relaxation rates and residual dipolar couplings.

Declaration of competing interest

The authors declare that they have no known competing financial interests or personal relationships that could have appeared to influence the work reported in this paper.

Data availability

Data will be made available on request.

Acknowledgments

Funding from the Bo Rydin Foundation (grant no F53/21) is gratefully acknowledged (ES).

Appendix A. Supplementary data

Supplementary data to this article can be found online at https://doi.org/10.1016/j.ssnmr.2024.101972.

References

[1] A.S. Michaels, S.K. Chandrasekaran, J.E. Shaw, Drug permeation through human skin: theory and in vitro experimental measurement, AlChE J. 21 (1975) 985–996, https://doi.org/10.1002/aic.690210522.
[2] E. Sparr, S. Björklund, Q.D. Pham, E.H. Mojumdar, B. Stenqvist, M. Gunnarsson, D. Topgaard, The stratum corneum barrier - from molecular scale to macroscopic properties, Curr. Opin. Colloid Interface Sci. 67 (2023) 101725, https://doi.org/10.1016/j.cocis.2023.101725.
[3] L. Norlén, Stratum corneum keratin structure, function and formation - a comprehensive review, Int. J. Cosmet. Sci. 28 (2006) 397–425, https://doi.org/10.1111/j.1467-2494.2006.00345.x.
[4] J.A. Bouwstra, G.S. Gooris, F.E.R. Dubbelaar, A.M. Weerheim, A.P. Ijzerman, M. Ponec, Role of ceramide 1 in the molecular organization of the stratum corneum lipids, J. Lipid Res. 39 (1998) 186–196, https://doi.org/10.1016/s0022-2275(20)34214-0.
[5] L. Norlén, M. Lundborg, C. Wennberg, A. Narangifard, B. Daneholt, The skin's barrier: a cryo-EM based overview of its architecture and stepwise formation, J. Invest. Dermatol. 142 (2022) 285–292, https://doi.org/10.1016/j.jid.2021.06.037.
[6] Y. Jokura, S. Ishikawa, H. Tokuda, G. Imokawa, Molecular analysis of elastic properties of the stratum corneum by solid-state ^{13}C-nuclear magnetic resonance spectroscopy, J. Invest. Dermatol. 104 (1995) 806–812, https://doi.org/10.1111/1523-1747.ep12607005.
[7] I. Matlahov, P.C.A. van der Wel, Hidden motions and motion-induced invisibility: dynamics-based spectral editing in solid-state NMR, Methods 148 (2018) 123–135, https://doi.org/10.1016/j.ymeth.2018.04.015.
[8] D. Topgaard, Skin, soap, and spaghetti: investigations of co-existing solid and liquid phases in organic materials using solid-state NMR with dynamics-based spectral editing, Pure Appl. Chem. 95 (2023) 1075–1089, https://doi.org/10.1515/pac-2023-0108.
[9] S. Björklund, T. Ruzgas, A. Nowacka, I. Dahi, D. Topgaard, E. Sparr, J. Engblom, Skin membrane electrical impedance properties under the influence of a varying water gradient, Biophys. J. 104 (2013) 2639–2650, https://doi.org/10.1016/j.bpj.2013.05.008.
[10] Q.D. Pham, S. Gregoire, B. Biatry, G. Cassin, D. Topgaard, E. Sparr, Skin hydration as a tool to control the distribution and molecular effects of intermediate polarity compounds in intact stratum corneum, J. Colloid Interface Sci. 603 (2021) 874–885, https://doi.org/10.1016/j.jcis.2021.06.097.
[11] S. Björklund, A. Nowacka, J.A. Bouwstra, E. Sparr, D. Topgaard, Characterization of stratum corneum molecular dynamics by natural-abundance ^{13}C solid-state NMR, PLoS One 8 (2013) e61889, https://doi.org/10.1371/journal.pone.0061889.
[12] S. Björklund, J.M. Andersson, A.E. Nowacka, Q.D. Pham, D. Topgaard, E. Sparr, Stratum corneum molecular mobility in the presence of natural moisturizers, Soft Matter 10 (2014) 4535–4546, https://doi.org/10.1039/C4SM00137K.
[13] E.H. Mojumdar, E. Sparr, The effect of pH and salt on the molecular structure and dynamics of the skin, Colloids Surf., B 198 (2021) 111476, https://doi.org/10.1016/j.colsurfb.2020.111476.
[14] M. Gunnarsson, E.H. Mojumdar, D. Topgaard, E. Sparr, Extraction of natural moisturizing factor from the stratum corneum and its implication on skin molecular mobility, J. Colloid Interface Sci. 604 (2021) 480–491, https://doi.org/10.1016/j.jcis.2021.07.012.
[15] Y. Sonoki, Q.D. Pham, E. Sparr, Beyond additivity: a mixture of glucose and NaCl can influence skin hydration more than the individual compounds, J. Colloid Interface Sci. 613 (2022) 554–562, https://doi.org/10.1016/j.jcis.2021.12.166.
[16] S. Björklund, Q.D. Pham, L.B. Jensen, N.O. Knudsen, L.D. Nielsen, K. Ekelund, T. Ruzgas, J. Engblom, E. Sparr, The effects of polar excipients transcutol and dexpanthenol on molecular mobility, permeability, and electrical impedance of the skin barrier, J. Colloid Interface Sci. 479 (2016) 207–220, https://doi.org/10.1016/j.jcis.2016.06.054.
[17] Q.D. Pham, S. Björklund, J. Engblom, D. Topgaard, E. Sparr, Chemical penetration enhancers in stratum corneum - relation between molecular effects and barrier function, J. Controlled Release 232 (2016) 175–187, https://doi.org/10.1016/j.jconrel.2016.04.030.
[18] N. Kis, M. Gunnarsson, S. Berko, E. Sparr, The effects of glycols on molecular mobility, structure, and permeability in stratum corneum, J. Controlled Release 343 (2022) 755–764, https://doi.org/10.1016/j.jconrel.2022.02.007.
[19] Q.D. Pham, D. Topgaard, E. Sparr, Tracking solvents in the skin through atomically resolved measurements of molecular mobility in intact stratum corneum, Proc. Natl. Acad. Sci. USA 114 (2017) E112–E121, https://doi.org/10.1073/pnas.1608739114.
[20] J. Bouwstra, F. Dubbelaar, G. Gooris, M. Ponec, The lipid organisation in the skin barrier, Acta Derm. Venereol. 80 (2000).
[21] J.A. Bouwstra, G.S. Gooris, F.E. Dubbelaar, M. Ponec, Phase behavior of stratum corneum lipid mixtures based on human ceramides: the role of natural and synthetic ceramide 1, J. Invest. Dermatol. 118 (2002) 606–617, https://doi.org/10.1046/j.1523-1747.2002.01706.x.
[22] J.A. Bouwstra, G.S. Gooris, F.E.R. Dubbelaar, M. Ponec, Phase behavior of lipid mixtures based on human ceramides: coexistence of crystalline and liquid phases, J. Lipid Res. 42 (2001) 1759–1770.
[23] Q.D. Pham, E.H. Mojumdar, G.S. Gooris, J.A. Bouwstra, E. Sparr, D. Topgaard, Solid and fluid segments within the same molecule of stratum corneum ceramide lipid, Q. Rev. Biophys. 51 (2018) e7, https://doi.org/10.1017/S0033583518000069.

[24] A. Paz Ramos, G. Gooris, J. Bouwstra, M. Lafleur, Evidence of hydrocarbon nanodrops in highly ordered stratum corneum model membranes, J. Lipid Res. 59 (2018) 137–143, https://doi.org/10.1194/jlr.M080432.
[25] O. Engberg, A. Kovacik, P. Pullmannova, M. Juhascik, L. Opalka, D. Huster, K. Vavrova, The sphingosine and acyl chains of ceramide [NS] show very different structure and dynamics that challenge our understanding of the skin barrier, Angew. Chem. Int. Ed. Engl. 59 (2020) 17383–17387, https://doi.org/10.1002/anie.202003375.
[26] F. Fandrei, O. Engberg, L. Opalka, P. Jancalkova, P. Pullmannova, M. Steinhart, A. Kovacik, K. Vavrova, D. Huster, Cholesterol sulfate fluidizes the sterol fraction of the stratum corneum lipid phase and increases its permeability, J. Lipid Res. 63 (2022) 100177, https://doi.org/10.1016/j.jlr.2022.100177.
[27] F. Fandrei, T. Havrisak, L. Opalka, O. Engberg, A. Smith, P. Pullmannova, N. Kucerka, V. Ondrejcekova, B. Deme, L. Novakova, M. Steinhart, K. Vavrova, D. Huster, The intriguing molecular dynamics of Cer[EOS] in rigid skin barrier lipid layers requires improvement of the model, J. Lipid Res. (2023) 100356, https://doi.org/10.1016/j.jlr.2023.100356.
[28] E. Wang, J.B. Klauda, Molecular structure of the long periodicity phase in the stratum corneum, J. Am. Chem. Soc. 141 (2019) 16930–16943, https://doi.org/10.1021/jacs.9b08995.
[29] H. Kovacs, D. Moskau, M. Spraul, Cryogenically cooled probes—a leap in NMR technology, Prog. Nucl. Magn. Reson. Spectrosc. 46 (2005) 131–155, https://doi.org/10.1016/j.pnmrs.2005.03.001.
[30] A. Hassan, C.M. Quinn, J. Struppe, I.V. Sergeyev, C. Zhang, C. Guo, B. Runge, T. Theint, H.H. Dao, C.P. Jaroniec, M. Berbon, A. Lends, B. Habenstein, A. Loquet, R. Kuemmerle, B. Perrone, A.M. Gronenborn, T. Polenova, Sensitivity boosts by the CPMAS CryoProbe for challenging biological assemblies, J. Magn. Reson. 311 (2020) 106680, https://doi.org/10.1016/j.jmr.2019.106680.
[31] Y. Du, J. Struppe, B. Perrone, A. Hassan, A. Codina, Y. Su, Efficient analysis of pharmaceutical drug substances and products using a solid-state NMR CryoProbe, Analyst 148 (2023) 724–734, https://doi.org/10.1039/d2an01903e.
[32] T. Gopinath, K. Shin, Y. Tian, W. Im, J. Struppe, B. Perrone, A. Hassan, F. M. Marassi, Solid-state NMR MAS CryoProbe enables structural studies of human blood protein vitronectin bound to hydroxyapatite, J. Struct. Biol. 216 (2024) 108061, https://doi.org/10.1016/j.jsb.2024.108061.
[33] G. Plewig, R.R. Marples, Regional differences of cell sizes in the human stratum corneum. Part I, J. Invest. Dermatol. 54 (1970) 13–18, https://doi.org/10.1111/1523-1747.ep12551482.
[34] M.M. Mershon, Barrier surfaces of skin, in: R.E. Baier (Ed.), Applied Chemistry at Protein Interfaces, American Chemical Society, 1975, pp. 41–73, https://doi.org/10.1021/ba-1975-0145.ch003.
[35] P.M. Elias, D.S. Friend, The permeability barrier in mammalian epidermis, J. Cell Biol. 65 (1975) 180–191, https://doi.org/10.1083/jcb.65.1.180.
[36] A. Pines, J.S. Waugh, M.G. Gibby, Proton enhanced nuclear induction spectroscopy - method for high-resolution NMR of dilute spins in solids, J. Chem. Phys. 56 (1972) 1776–1777, https://doi.org/10.1063/1.1677439.
[37] G. Metz, X. Wu, S.O. Smith, Ramped-amplitude cross polarization in magic-angle-spinning NMR, J. Magn. Reson. 110 (1994) 219–227, https://doi.org/10.1006/jmra.1994.1208.
[38] G.A. Morris, R. Freeman, Enhancement of nuclear magnetic resonance signals by polarization transfer, J. Am. Chem. Soc. 101 (1979) 760–762, https://doi.org/10.1021/ja00497a058.
[39] D.P. Burum, R.R. Ernst, Net polarization transfer via a *J*-ordered state for signal enhancement of low-sensitivity nuclei, J. Magn. Reson. 39 (1980) 163–168, https://doi.org/10.1016/0022-2364(80)90168-7.
[40] A. Nowacka, N.A. Bongartz, O.H.S. Ollila, T. Nylander, D. Topgaard, Signal intensities in ^{1}H-^{13}C CP and INEPT MAS NMR of liquid crystals, J. Magn. Reson. 230 (2013) 165–175, https://doi.org/10.1016/j.jmr.2013.02.016.
[41] S. Kaplan, Compatibility of TPD/polycarbonate blends by carbon-13-proton HETCOR in the solid state, Macromolecules 26 (1993) 1060–1064, https://doi.org/10.1021/ma00057a028.
[42] K. Schmidt-Rohr, J. Clauss, B. Blümich, H.W. Spiess, Miscibility of polymer blends investigated by ^{1}H spin diffusion and ^{13}C NMR detection, Magn. Reson. Chem. 28 (1990) S3–S9, https://doi.org/10.1002/mrc.1260281304.
[43] J. Wang, On the determination of domain sizes in polymers by spin diffusion, J. Chem. Phys. 104 (1996) 4850–4858, https://doi.org/10.1063/1.471179.
[44] J. Clauss, K. Schmidt-Rohr, H.W. Spiess, Determination of domain sizes in heterogeneous polymers by solid-state NMR, Acta Polym. 44 (1993) 1–17, https://doi.org/10.1002/actp.1993.010440101.
[45] Z. Sun, S. Yuan, K. Schmidt-Rohr, Quantification of large long periods in rigid polymer systems by ^{1}H spin diffusion in HetCor NMR with heavy peak overlap, Appl. Magn. Reson. (2023), https://doi.org/10.1007/s00723-023-01570-7.
[46] B.M. Fung, A.K. Khitrin, K. Ermolaev, An improved broadband decoupling sequence for liquid crystals and solids, J. Magn. Reson. 142 (2000) 97–101, https://doi.org/10.1006/jmre.1999.1896.
[47] O. Soubias, V. Réat, O. Saurel, A. Milon, High resolution 2D ^{1}H-^{13}C correlation of cholesterol in model membrane, J. Magn. Reson. 158 (2002) 143–148, https://doi.org/10.1016/S1090-7807(02)00067-8.
[48] T.M. Ferreira, F. Coreta-Gomes, O.H.S. Ollila, M.J. Moreno, W.L.C. Vaz, D. Topgaard, Cholesterol and POPC segmental order parameters in lipid membranes: solid state ^{1}H-^{13}C NMR and MD simulation studies, Phys. Chem. Chem. Phys. 15 (2013) 1976–1989, https://doi.org/10.1039/C2CP42738A.
[49] A. Kisic, M. Tsuda, R.J. Kulmacz, W.K. Wilson, G.J. Schroepfer Jr., Sphingolipid bases. A revisitation of the O-methyl derivatives of sphingosine. Isolation and characterization of diacetate derivatives, with revised ^{13}C nuclear magnetic resonance assignments for D-erythro-sphingosine, J. Lipid Res. 36 (1995) 787–805, https://doi.org/10.1016/S0022-2275(20)40063-X.
[50] D. Bernin, E. Leventaki, D. Topgaard, Solid–liquid phase transitions of triglycerides in griebenschmalz, smalec, and fedt studied using ^{13}C solid-state NMR with dynamics-based spectral filtering, Appl. Magn. Reson. 54 (2023) 1165–1175, https://doi.org/10.1007/s00723-023-01564-5.
[51] W.L. Earl, D.L. VanderHart, Observations in solid polyethylenes by carbon-13 magnetic resonance with magic angle sample spinning, Macromolecules 12 (1979) 762–767, https://doi.org/10.1021/ma60070a045.
[52] H.R. Kricheldorf, D. Müller, Secondary structure of peptides 16th. Characterization of proteins by means of ^{13}C NMR CP/MAS spectroscopy, Colloid Polym. Sci. 262 (1984) 856–861, https://doi.org/10.1007/BF01452215.
[53] M.J. Duer, N. McDougal, R.C. Murray, A solid-state NMR study of the structure and molecular mobility of α-keratin, Phys. Chem. Chem. Phys. 5 (2003) 2894–2899, https://doi.org/10.1039/b302506c.
[54] Q.Z. Ni, E. Daviso, T.V. Can, E. Markhasin, S.K. Jawla, T.M. Swager, R.J. Temkin, J. Herzfeld, R.G. Griffin, High frequency dynamic nuclear polarization, Acc. Chem. Res. 46 (2013) 1933–1941, https://doi.org/10.1021/ar300348n.
[55] A. Bielecki, A.C. Kolbert, M.H. Levitt, Frequency-switched pulse sequences: homonuclear decoupling and dilute spin NMR in solids, Chem. Phys. Lett. 155 (1989) 341–346, https://doi.org/10.1016/0009-2614(89)87166-0.
[56] B. Efron, Nonparametric estimates of standard error: the jackknife, the bootstrap and other methods, Biometrika 68 (1981) 589–599, https://doi.org/10.2307/2335441.
[57] F. Mellinger, M. Wilhelm, H.W. Spiess, Calibration of ^{1}H NMR spin diffusion coefficients for mobile polymers through transverse relaxation measurements, Macromolecules 32 (1999) 4686–4691, https://doi.org/10.1021/ma9820265.